The Astrophysical Journal, 762:119 (9pp), 2013 January 10 doi:10.1088/0004-637X/762/2/119

PARALLAXES AND PROPER MOTIONS OF ULTRACOOL BROWN DWARFS OF SPECTRAL TYPES Y AND LATE T

Kenneth A. Marsh[1,2], Edward L. Wright[3], J. Davy Kirkpatrick[1], Christopher R. Gelino[1], Michael C. Cushing[4], Roger L. Griffith[1], Michael F. Skrutskie[5], and Peter R. Eisenhardt[6]
[1] Infrared Processing and Analysis Center, California Institute of Technology, Pasadena, CA 91125, USA
[2] School of Physics & Astronomy, Cardiff University, Cardiff CF24 3AA, UK; ken.marsh@astro.cf.ac.uk
[3] Department of Physics & Astronomy, UCLA, P.O. Box 951547, Los Angeles, CA 90095, USA
[4] Department of Physics & Astronomy, The University of Toledo, 2801 West Bancroft Street, Toledo, OH 43606, USA
[5] Department of Astronomy, University of Virginia, Charlottesville, VA 22904, USA
[6] NASA Jet Propulsion Laboratory, 4800 Oak Grove Drive, Pasadena, CA 91109, USA
Received 2012 May 4; accepted 2012 November 22; published 2012 December 21

ABSTRACT

We present astrometric measurements of 11 nearby ultracool brown dwarfs of spectral types Y and late-T, based on imaging observations from a variety of space-based and ground-based telescopes. These measurements have been used to estimate relative parallaxes and proper motions via maximum likelihood fitting of geometric model curves. To compensate for the modest statistical significance ($\lesssim$7) of our parallax measurements we have employed a novel Bayesian procedure for distance estimation which makes use of an a priori distribution of tangential velocities, $V_{\rm tan}$, assumed similar to that implied by previous observations of T dwarfs. Our estimated distances are therefore somewhat dependent on that assumption. Nevertheless, the results have yielded distances for five of our eight Y dwarfs and all three T dwarfs. Estimated distances in all cases are $\gtrsim$3 pc. In addition, we have obtained significant estimates of $V_{\rm tan}$ for two of the Y dwarfs; both are $<$100 km s^{-1}, consistent with membership in the thin disk population. Comparison of absolute magnitudes with model predictions as a function of color shows that the Y dwarfs are significantly redder in $J-H$ than predicted by a cloud-free model.

Key words: astrometry – brown dwarfs – stars: low-mass

Online-only material: color figures

1. INTRODUCTION

Determining accurate distances to brown dwarfs is important for a number of reasons. First, distance is a vital quantity in establishing not only the space density of these objects, but also the luminosity function which can then be used to test models of star formation at the lowest masses. Second, distances allow the spectra of brown dwarfs to be placed on an absolute flux scale to provide more quantitative checks of atmospheric models. Third, distances for the nearest objects allow us to construct a more complete view of our own solar neighborhood, allowing us to directly visualize the relative importance of brown dwarfs in the Galactic context. Sometimes, distance determinations produce results wholly unanticipated. For example, the *J*-band overluminosity of the T4.5 dwarf 2MASS J05591914−1404488 (Figure 2 of Dahn et al. 2002) was unexpected despite its location near the *J*-band bump at the L/T transition (e.g., Looper et al. 2008), a feature thought to be associated with decreasing cloudiness (Marley et al. 2010). It has been suggested, however, that the overluminosity is due to the presence of an unresolved binary (Burgasser et al. 2002; Dupuy & Liu 2012). Similarly unexpected was the recent determination that young, field L dwarfs are often significantly underluminous for their spectral types at near-infrared magnitudes (Faherty et al. 2012).

Some of the earliest parallax determinations for brown dwarfs were by Dahn et al. (2002), Tinney et al. (2003), Vrba et al. (2004), once surveys such as the Two Micron All-Sky Survey (2MASS; Skrutskie et al. 2006), the Sloan Digital Sky Survey (SDSS; York et al. 2000), and the Deep Near-infrared Survey of the southern sky (Epchtein et al. 1997) began to identify L and T dwarfs in large numbers. More recently, parallax programs by groups such as Marocco et al. (2010) and Dupuy & Liu (2012) have pushed astrometry measurements to the latest T spectral subclasses. With the discovery of Y dwarfs from *WISE* (Cushing et al. 2011; Kirkpatrick et al. 2012) we are now pushing these measurements to even colder temperatures (Beichman et al. 2012). In this paper, we present distance and/or proper motion measurements for an additional eight Y dwarfs, along with three nearby late-T dwarfs, and present the first tangential velocity measurements for Y dwarfs.

2. OBSERVATIONS

Our set of objects includes all known Y dwarfs for which we have imaging data at a sufficient number of epochs for parallax and proper motion estimation. The exception is WISE 1828+2650, presented separately by Beichman et al. (2012). In addition, we have included three late T dwarfs from an investigation of the low-mass end of the substellar mass function within 8 pc of the Sun (Kirkpatrick et al. 2011). The complete sample is listed in the observing log shown in Table 1.

Each of these objects has been observed at two or three epochs by the *Wide-field Infrared Survey Explorer* (*WISE*; Wright et al. 2010) and at least four more epochs of imaging observations by the IRAC instrument (Fazio et al. 2004) on the *Spitzer Space Telescope* (*Spitzer*; Werner et al. 2004), the WFC3 instrument (Straughn et al. 2011) of the *Hubble Space Telescope* (*HST*), and various ground-based observatories. The observatories and instruments used are listed in the footnote of Table 1, and further details are given by Kirkpatrick et al. (2011, 2012).

3. ASTROMETRY MEASUREMENT PROCEDURE

Astrometric information was extracted from the observed images at the various epochs using the standard maximum likelihood technique in which a point-spread function (PSF) is fit

Table 1
Observing Log and Relative Astrometry Measurements

Object	Sp	R.A. (nom) (°)	Decl. (nom) (°)	Instrument	Band	Date	Elongation (°)	$\Delta\alpha \cos\delta$ (″)	$\Delta\delta$ (″)
WISE J035000.32−565830.2	Y1	57.501375	−56.975006	*WISE*	*W*2	2010 Jul 9	−89.9	−0.153 (0.232)	−0.062 (0.208)
				Spitzer	[4.5]	2010 Sep 18	−158.2	−0.131 (0.119)	−0.126 (0.156)
				PANIC	*J*	2010 Nov 25	134.2	−0.314 (0.279)	−0.562 (0.182)
				WISE	*W*2	2011 Jan 2	95.5	−0.743 (0.221)	−1.094 (0.215)
				Spitzer	[4.5]	2011 Jan 19	78.2	−0.927 (0.309)	−1.486 (0.273)
				HST	*J*	2011 Aug 13	−123.2	−0.271 (0.094)	−0.857 (0.062)
				Spitzer	[4.5]	2011 Nov 20	139.5	−0.378 (0.129)	−1.148 (0.131)
				Spitzer	[4.5]	2012 Mar 20	17.0	−0.722 (0.137)	−1.808 (0.075)
WISE J035934.06−540154.6	Y0	59.892083	−54.031703	*WISE*	*W*2	2010 Jan 13	93.4	−0.203 (0.298)	−0.200 (0.316)
				WISE	*W*2	2010 Jul 18	−89.2	−0.273 (0.278)	−0.867 (0.287)
				PANIC	*J*	2010 Aug 1	−102.6	−0.434 (0.145)	−0.907 (0.166)
				Spitzer	[4.5]	2010 Sep 18	−148.9	−0.468 (0.267)	−0.632 (0.251)
				PANIC	*H*	2010 Nov 25	143.5	−0.521 (0.052)	−0.987 (0.144)
				WISE	*W*2	2011 Jan 11	95.7	−0.374 (0.295)	−1.169 (0.301)
				Spitzer	[4.5]	2011 Jan 19	87.5	−0.500 (0.196)	−1.284 (0.237)
				HST	*J*	2011 Aug 9	−110.0	−0.521 (0.039)	−1.499 (0.040)
				Spitzer	[4.5]	2011 Nov 20	148.8	−0.564 (0.194)	−1.969 (0.085)
				Spitzer	[4.5]	2012 Mar 20	26.3	−1.036 (0.113)	−2.147 (0.178)
WISEP J041022.71+150248.5	Y0	62.594667	15.046819	*WISE*	*W*2	2010 Feb 16	96.3	−0.001 (0.188)	−0.052 (0.222)
				WISE	*W*2	2010 Aug 26	−89.2	0.945 (0.168)	−1.083 (0.193)
				WIRC	*J*	2010 Aug 29	−92.1	0.997 (0.172)	−0.965 (0.258)
				Spitzer	[4.5]	2010 Oct 21	−144.0	1.411 (0.066)	−1.538 (0.050)
				Spitzer	[4.5]	2011 Apr 14	39.7	1.175 (0.134)	−2.621 (0.090)
				Spitzer	[4.5]	2011 Nov 19	−172.8	2.134 (0.134)	−3.894 (0.079)
				Spitzer	[4.5]	2012 Mar 20	63.7	2.320 (0.126)	−4.417 (0.132)
WISE J053516.80−750024.9	⩾Y1	83.820042	−75.007019	*WISE*	*W*2	2010 Mar 31	−89.5	−0.361 (0.284)	0.458 (0.317)
				WISE	*W*2	2010 Sep 28	95.9	0.172 (0.266)	0.693 (0.182)
				Spitzer	[4.5]	2010 Oct 17	77.1	−0.006 (0.151)	1.221 (0.099)
				Spitzer	[4.5]	2011 Apr 17	−106.0	−0.582 (0.145)	1.337 (0.160)
				HST	*J*	2011 Sep 27	97.1	−0.284 (0.086)	1.112 (0.036)
				Spitzer	[4.5]	2011 Nov 20	43.3	−0.297 (0.093)	1.223 (0.137)
WISEPC J140518.40+553421.5	Y0p?	211.326667	55.572628	*WISE*	*W*2	2010 Jun 8	96.0	−0.165 (0.145)	0.107 (0.198)
				WIRC	*J*	2010 Jul 26	50.2	−0.828 (0.401)	0.013 (0.216)
				WISE	*W*2	2010 Dec 14	−88.8	−1.388 (0.161)	−0.050 (0.284)
				Spitzer	[4.5]	2011 Jan 22	−128.5	−1.829 (0.130)	−0.210 (0.125)
				HST	*J*	2011 Mar 14	−180.0	−1.723 (0.118)	0.155 (0.171)
				Spitzer	[4.5]	2012 Feb 21	−158.6	−4.002 (0.445)	0.323 (0.203)
				Spitzer	[4.5]	2012 Jun 22	82.1	−4.862 (0.148)	0.260 (0.412)
WISE J154151.65−225024.9	Y0.5	235.465250	−22.840358	*WISE*	*W*2	2010 Feb 17	−89.8	0.206 (0.532)	−0.209 (0.708)
				WISE	*W*2	2010 Aug 15	96.4	0.041 (0.175)	−0.093 (0.173)
				FIRE	*J*	2011 Mar 27	−127.5	−0.959 (0.196)	−0.351 (0.198)
				Spitzer	[4.5]	2011 Apr 13	−144.3	−1.019 (0.120)	−0.418 (0.140)
				NEWFIRM	*J*	2011 Apr 17	−148.2	−1.340 (0.566)	−0.430 (0.682)
				MMIRS	*J*	2011 May 14	−174.4	−1.260 (0.113)	−0.292 (0.128)
				Spitzer	[4.5]	2012 Apr 28	−159.7	−2.028 (0.101)	−0.568 (0.144)
WISE J173835.53+273259.0	Y0	264.648083	27.549758	*WISE*	*W*2	2010 Mar 14	−90.8	−0.136 (0.188)	0.036 (0.204)
				WIRC	*J*	2010 Jul 26	139.5	−0.009 (0.074)	−0.314 (0.060)
				WIRC	*J*	2010 Aug 29	106.9	−0.154 (0.271)	0.046 (0.266)
				WISE	*W*2	2010 Sep 9	96.3	−0.064 (0.174)	−0.309 (0.200)
				Spitzer	[4.5]	2010 Sep 18	87.5	−0.075 (0.103)	−0.465 (0.110)
				HST	*J*	2011 May 12	−148.5	0.291 (0.056)	−0.613 (0.048)
				Spitzer	[4.5]	2011 May 20	−156.2	0.336 (0.171)	−0.544 (0.174)
				Spitzer	[4.5]	2011 Nov 26	19.1	0.276 (0.138)	−0.982 (0.082)
				Spitzer	[4.5]	2012 May 12	−149.2	0.734 (0.124)	−0.765 (0.109)
WISEPC J205628.90+145953.3	Y0	314.120417	14.998147	*WISE*	*W*2	2010 May 13	−90.6	0.027 (0.172)	0.042 (0.167)
				WIRC	*J*	2010 Aug 29	166.0	−0.100 (0.168)	0.316 (0.170)
				WISE	*W*2	2010 Nov 8	96.1	−0.015 (0.135)	0.163 (0.144)
				Spitzer	[4.5]	2010 Dec 10	63.8	0.354 (0.148)	0.437 (0.160)
				Spitzer	[4.5]	2011 Jul 6	−142.0	1.087 (0.229)	0.853 (0.146)
				HST	*J*	2011 Sep 4	160.5	0.933 (0.035)	0.810 (0.083)
				Spitzer	[4.5]	2012 Jan 6	36.5	1.152 (0.203)	0.936 (0.231)
				Spitzer	[4.5]	2012 Jul 18	−154.2	1.889 (0.032)	1.332 (0.042)
WISEPA J025409.45+022359.1	T8	43.539375	2.399750	*WISE*	*W*2	2010 Jan 27	94.9	0.052 (0.085)	−0.745 (0.119)
				WISE	*W*2	2010 Aug 5	−90.7	1.673 (0.139)	−0.509 (0.100)

Table 1
(Continued)

Object	Sp	R.A. (nom) (°)	Decl. (nom) (°)	Instrument	Band	Date	Elongation (°)	$\Delta\alpha\cos\delta$ (″)	$\Delta\delta$ (″)
				WIRC	*H*	2010 Aug 29	−113.7	1.839 (0.144)	−0.514 (0.181)
				WIRC	*J*	2010 Aug 29	−113.7	1.864 (0.120)	−0.546 (0.189)
				Spitzer	[4.5]	2010 Sep 17	−132.2	2.164 (0.110)	−0.536 (0.064)
				WISE	*W*2	2011 Jan 27	95.1	2.349 (0.193)	−0.306 (0.231)
				Spitzer	[4.5]	2011 Mar 2	60.8	2.868 (0.068)	−0.411 (0.126)
				Spitzer	[4.5]	2012 Mar 7	55.0	5.504 (0.049)	−0.162 (0.067)
WISEPC J150649.97+702736.0	T6	226.708208	70.460000	*WISE*	*W*2	2010 May 12	95.4	−0.101 (0.106)	−0.010 (0.118)
				WIRC	*H*	2010 Aug 29	−9.0	−0.479 (0.083)	0.064 (0.065)
				WIRC	*J*	2010 Aug 29	−9.0	−0.467 (0.082)	0.086 (0.059)
				WISE	*W*2	2010 Nov 18	−89.0	−0.488 (0.119)	0.069 (0.220)
				Spitzer	[4.5]	2010 Dec 22	−123.5	−0.573 (0.069)	−0.005 (0.065)
				Spitzer	[4.5]	2011 Apr 23	114.0	−0.707 (0.077)	0.990 (0.136)
				Spitzer	[4.5]	2012 Jan 23	−155.8	−2.192 (0.307)	1.377 (0.292)
				Spitzer	[4.5]	2012 May 25	82.4	−2.278 (0.148)	2.130 (0.115)
WISEPA J174124.26+255319.5	T9	265.351083	25.888750	2MASS	*J*	2000 Apr 11	−117.8	−0.069 (0.138)	0.188 (0.104)
				SDSS	*z*	2004 Sep 16	90.1	2.320 (0.087)	8.248 (0.104)
				WISE	*W*2	2010 Mar 15	−90.7	0.114 (0.261)	0.125 (0.099)
				PAIRITEL	*H*	2010 Apr 9	−115.4	−0.194 (0.082)	0.109 (0.109)
				FanMt	*J*	2010 Apr 10	−116.4	−0.136 (0.038)	0.231 (0.058)
				FanMt	*H*	2010 Apr 10	−116.4	−0.103 (0.100)	0.240 (0.064)
				WISE	*W*2	2010 Sep 10	96.4	−0.582 (0.132)	−0.596 (0.184)
				Spitzer	[4.5]	2010 Sep 18	88.6	−0.679 (0.143)	−0.334 (0.179)
				Spitzer	[4.5]	2011 May 20	−155.1	−0.463 (0.184)	−1.317 (0.200)
				Spitzer	[4.5]	2011 Nov 20	26.3	−1.265 (0.052)	−2.312 (0.059)
				Spitzer	[4.5]	2012 May 8	−144.2	−1.132 (0.088)	−2.977 (0.073)

Notes. The columns represent the object name, spectral type from Cushing et al. (2011); Kirkpatrick et al. (2012), nominal R.A. and decl. position (J2000), the instrument (or telescope), band, UT date of observation, solar elongation angle, and the measured positional offsets (in R.A. and decl.) of the source from its nominal position. The key to the entries in the instrument column is as follows: *WISE* = *Wide-field Infrared Survey Explorer* (Wright et al. 2010); *HST* = WFC3 camera on the *Hubble Space Telescope* (Straughn et al. 2011); *Spitzer* = Infrared Array Camera (IRAC) on *Spitzer* (Werner et al. 2004); FanMt = Fan Mountain Near-infrared Camera (FanCam) (Kanneganti et al. 2009); FIRE = Folded-port Infrared Echellette at Las Campanas Observatory (Simcoe et al. 2008, 2010); MMIRS = MMT and Magellan Infrared Spectrograph (McLeod et al. 2004); NEWFIRM = NOAO Extremely Wide-Field Infrared Imager at Cerro Tololo (Swaters et al. 2009); PANIC = Persson's Auxiliary Nasmyth Infrared Camera at Las Campanas Observatory (Martini et al. 2004); PAIRITEL = Peters Automated Infrared Imaging Telescope on Mt. Hopkins (Bloom et al. 2006); SDSS = Sloan Digital Sky Survey (York et al. 2000); 2MASS = Two Micron All Sky Survey (Cutri et al. 2003); WIRC = Wide-field Infrared Camera on the 5 m Hale Telescope (Wilson et al. 2003).

to each observed source profile. The technique was essentially the same as used in 2MASS, the details of which are given by Cutri et al. (2003), except that the source extraction results presented here were made using co-added images rather than focal-plane images. The positional uncertainties were estimated using an error model which includes the effects of instrumental and sky background noise and PSF uncertainty. The PSF and its associated uncertainty map were estimated for each image individually using a set of bright stars in the field, the median number for which was 14. Since the co-added images were Nyquist sampled or better, sinc interpolation was appropriate during PSF estimation and subsequent profile fitting to the data.

In order to minimize the systematic effects of focal-plane distortion and plate scale and rotation errors, our astrometry is based on relative positions using a reference star (or set of reference stars) in the vicinity of the object. For most objects we were able to find a reference star within ∼10″ common to all images except for those of *WISE*, due to the lower sensitivity of the latter. In order to incorporate the *WISE* data it has therefore been necessary to include bright reference stars which in general were much more widely separated from the brown dwarf (up to ∼100″). Most of these were taken from the 2MASS Point Source Catalog (Cutri et al. 2003). In order not to let these stars significantly compromise the astrometry measurements from the more sensitive images with close reference stars, we used a hybrid scheme in which the bright stars were treated as secondary references, bootstrapped to the close reference stars using the images in which they were in common.

The procedure is based on the following measurement model for the observed separation between the brown dwarf and reference star:

$$\alpha_t - \alpha_{it}^{\rm ref} = \alpha_t^{\rm BD} - \left(\alpha_i^{\rm cat} + \Delta\alpha_i^{\rm cat}\right) + \nu_t - \nu_{it} \quad (1)$$

$$\delta_t - \delta_{it}^{\rm ref} = \delta_t^{\rm BD} - \left(\delta_i^{\rm cat} + \Delta\delta_i^{\rm cat}\right) + \nu'_t - \nu'_{it}, \quad (2)$$

where α_t, δ_t and $\alpha_{it}^{\rm ref}, \delta_{it}^{\rm ref}$ represent the extracted positions of the brown dwarf and *i*th reference star, respectively, estimated from the image at epoch *t* based on the nominal position calibration of that image; $\alpha_i^{\rm cat}, \delta_i^{\rm cat}$ represent the catalog position of the reference star, and $\Delta\alpha_i^{\rm cat}, \Delta\delta_i^{\rm cat}$ represent errors in the catalog position; ν_t, ν'_t represent the estimation errors for the brown dwarf, and ν_{it}, ν'_{it} represent the estimation errors for the reference star. These estimation errors include the effects of random measurement noise on the source extraction as well as the residual effects of focal-plane distortion in the position differences. We assume that they can all be described by zero-mean Gaussian random processes.

If we further assume that the $\Delta\alpha_i^{\rm cat}, \Delta\delta_i^{\rm cat}$ are described a priori by zero-mean Gaussian random processes with standard deviations substantially larger than the extraction uncertainties of the reference stars, then an optimal estimate of the brown

dwarf position can be obtained from

$$\hat{\alpha}_t^{\rm BD} = \alpha_t + \frac{1}{N_t}\sum_{i\in\mathcal{R}(t)}\left(\alpha_i^{\rm cat} - \alpha_{it}^{\rm ref}\right) \quad (3)$$

$$\hat{\delta}_t^{\rm BD} = \delta_t + \frac{1}{N_t}\sum_{i\in\mathcal{R}(t)}\left(\delta_i^{\rm cat} - \delta_{it}^{\rm ref}\right), \quad (4)$$

where $\mathcal{R}(t)$ is the set of detected reference stars in the image at epoch t, and N_t is the number of stars in the set.

The resulting estimates are included in Table 1 in the form of offsets from the nominal position of the brown dwarf at each epoch, and the set of reference stars used is given in Table 2. After having obtained $\hat{\alpha}_t^{\rm BD}$ and $\hat{\delta}_t^{\rm BD}$, the individual reference star catalog errors can then be estimated using

$$\hat{\Delta\alpha}_i^{\rm cat} = -\alpha_i^{\rm cat} + \frac{1}{N_i}\sum_{t\in\mathcal{E}(i)}\left(\hat{\alpha}_t^{\rm BD} + \alpha_{it}^{\rm ref} - \alpha_t\right) \quad (5)$$

$$\hat{\Delta\delta}_i^{\rm cat} = -\delta_i^{\rm cat} + \frac{1}{N_i}\sum_{t\in\mathcal{E}(i)}\left(\hat{\delta}_t^{\rm BD} + \delta_{it}^{\rm ref} - \delta_t\right), \quad (6)$$

where $\mathcal{E}(i)$ is the set of all epochs for which the ith reference star is detected in the corresponding image, and N_i is the number of epochs in the set.

These values can be applied as corrections to the catalog positions of the reference stars, enabling a corresponding time series of estimated brown dwarf positions to be obtained separately for each individual reference star via Equations (1) and (2). The scatter in these estimates then provides a check on the assumptions regarding systematic effects such as focal-plane distortion and possible small proper motions of the reference stars themselves. We have included the effect of this scatter in the final quoted error bars in Table 1.

4. ESTIMATION OF PARALLAX AND PROPER MOTION

The measurement model incorporated the effects of parallax and linear proper motion, with appropriate correction for the Earth-trailing orbit in the case of *Spitzer* observations. The equations used (Kirkpatrick et al. 2011) were as follows:

$$\cos\delta_1(\alpha_i - \alpha_1) = \Delta\alpha + \mu_\alpha(t_i - t_1) + \pi_{\rm trig}\boldsymbol{R}_i\cdot\hat{W} \quad (7)$$

$$\delta_i - \delta_1 = \Delta\delta + \mu_\delta(t_i - t_1) - \pi_{\rm trig}\boldsymbol{R}_i\cdot\hat{N}, \quad (8)$$

where t_i is the observation time [yr] of the ith astrometric measurement, and R_i is the vector position of the observer relative to the Sun in celestial coordinates and astronomical units. $\hat{N}$ and $\hat{W}$ are unit vectors pointing north and west from the position of the source. R_i is the position of the Earth for 2MASS, SDSS, *WISE*, and *HST* observations; for *Spitzer* observations, R_i is the position of the spacecraft. The observed positional difference on the left-hand side is in arcseconds, the parameters $\Delta\alpha$ and $\Delta\delta$ are in arcseconds, the proper motion μ_α and μ_δ are in arcseconds yr^{-1}, and the parallax $\pi_{\rm trig}$ is in arcseconds.

Maximum likelihood estimates, based on the assumption of Gaussian measurement noise, were made of five parameters: the R.A. and decl. position offsets of the source at a specified reference time, the R.A. and decl. rates of proper motion, and the parallax. The uncertainties were derived using the standard procedure for maximum likelihood estimation (Whalen

Table 2
Reference Stars Used

Object	Sp	R.A.(ref) (°)	Decl.(ref) (°)	Separation (″)	Comment
WISE 0350−5658	Y1	57.505458	−56.976833	10.4	
		57.498042	−56.985000	36.6	2MASS
		57.493500	−56.961917	49.6	2MASS
		57.469708	−56.975861	62.2	2MASS
		57.520292	−56.993056	74.8	2MASS
		57.539625	−56.972556	75.6	2MASS
WISE 0359−5401	Y0	59.895458	−54.033444	9.5	
		59.894458	−54.021056	38.7	2MASS
		59.908333	−54.042639	52.3	2MASS
		59.932417	−54.040583	91.1	2MASS
WISE 0410+1502	Y0	62.600125	15.058056	44.7	2MASS
		62.580167	15.039056	57.6	2MASS
		62.607333	15.034722	62.0	2MASS
		62.618333	15.049167	82.7	2MASS
		62.607083	15.023306	95.0	2MASS
		62.622125	15.043389	96.3	2MASS
WISE 0535−7500	⩾Y1	83.824208	−75.009278	9.0	
		83.793542	−75.004417	26.4	2MASS
		83.811542	−74.998583	31.4	2MASS
		83.771250	−75.010028	46.7	2MASS
		83.769292	−75.004389	48.2	2MASS
		83.823500	−74.990444	59.7	2MASS
WISE 1405+5534	Y0p?	211.327083	55.574778	7.8	
		211.343208	55.584722	55.0	
		211.305583	55.585333	62.7	
		211.273042	55.574167	109.3	2MASS
		211.380417	55.576639	110.4	2MASS
WISE 1541−2250	Y0.5	235.464417	−22.836833	13.0	2MASS
		235.466750	−22.831694	31.6	2MASS
		235.473958	−22.848833	42.0	2MASS
		235.477375	−22.845306	44.0	2MASS
		235.482167	−22.843861	57.5	2MASS
		235.467875	−22.857306	61.6	2MASS
WISE 1738+2732	Y0	264.643542	27.547750	16.2	2MASS
		264.657750	27.554444	35.2	2MASS
		264.640292	27.535667	56.5	2MASS
		264.657750	27.534028	64.5	2MASS
		264.640917	27.530556	72.8	2MASS
		264.652417	27.572083	81.5	2MASS
WISE 2056+1459	Y0	314.117042	15.000111	13.7	2MASS
		314.118667	15.002556	17.0	2MASS
		314.120417	15.007694	34.3	2MASS
		314.132917	14.993361	46.8	2MASS
		314.106625	14.999250	48.1	2MASS
		314.123833	15.014750	60.9	2MASS
WISE 0254+0223	T8	43.540792	2.412833	47.3	2MASS
		43.537250	2.386722	47.5	2MASS
		43.557958	2.400333	66.9	2MASS
		43.512667	2.395778	97.1	2MASS
WISE 1506+7027	T6	226.736375	70.461806	34.5	2MASS
		226.677125	70.475250	66.4	2MASS
		226.750958	70.443639	78.3	2MASS
		226.658042	70.478833	90.8	2MASS
WISE 1741+2553	T9	265.355375	25.896583	31.4	2MASS
		265.341375	25.893556	35.9	2MASS
		265.332083	25.883611	64.2	2MASS
		265.360417	25.905361	67.1	2MASS
		265.346958	25.869194	71.7	2MASS
		265.339750	25.905861	71.7	2MASS

Note. Columns represent the object name, spectral type, the R.A. and decl. values of the associated reference stars, their separations from the object, and a comment column indicating which of the reference stars are in the Two Micron All-Sky Survey (2MASS) point-source catalog.

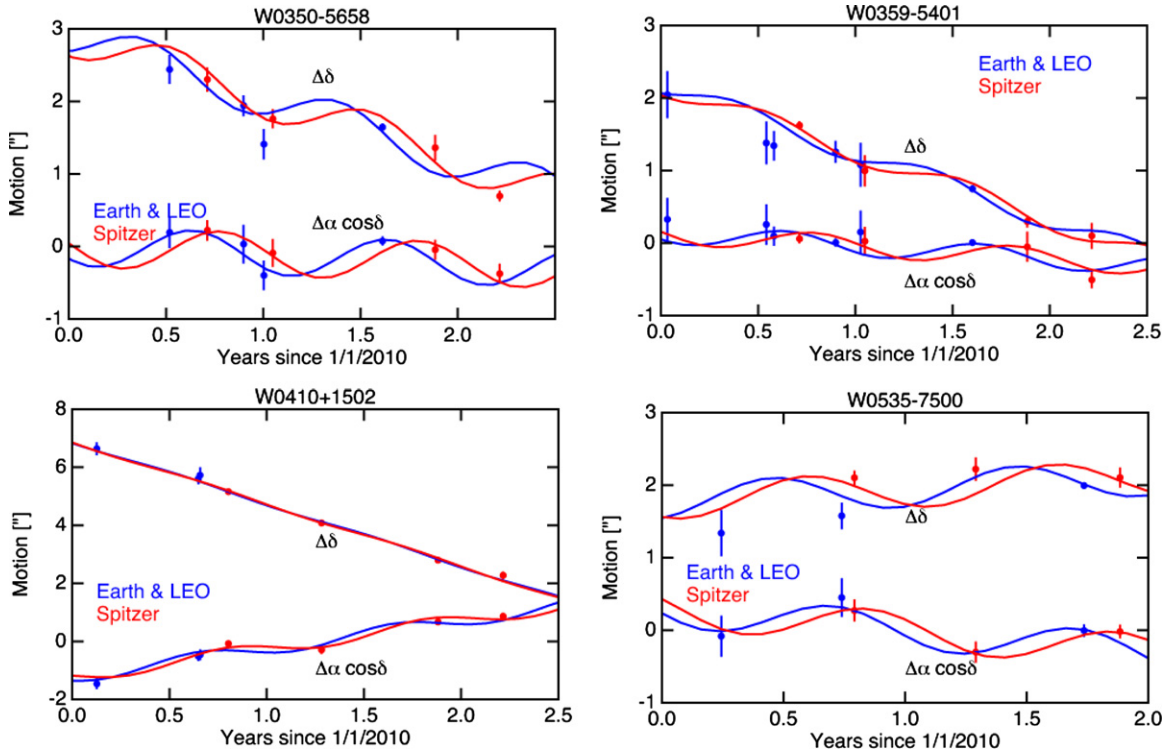

Figure 1. Proper motion and parallax fits to astrometry measurements of four of the Y dwarfs. Blue symbols represent observations from the ground and Low Earth Orbit (LEO), and red symbols represent *Spitzer* observations. The blue and red curves represent the corresponding model fits, respectively. The origins for the position offsets on the vertical (motion) axes have been adjusted with respect to the values in Table 1; the $\Delta\delta$ and $\Delta\alpha \cos\delta$ values are relative to a constant position fit, so they are relative to the weighted mean of the α and δ. In addition, the $\Delta\delta$ values are offset for clarity by different amounts for the different plots.

(A color version of this figure is available in the online journal.)

Table 3
Parallax and Proper Motion Estimates

Object	Sp	χ^2	$N_{\rm df}$	$\mu_\alpha \cos\delta$ ($''$ yr^{-1})	μ_δ ($''$ yr^{-1})	π ($''$)	Significance (sigmas)	d (pc)	$V_{\rm tan}$ (km s^{-1})
WISE 0350−5658	Y1	14.22	11	-0.125 ± 0.097	-0.865 ± 0.076	0.291 ± 0.050	5.8	$3.7^{+1.6}_{-0.4}$	18 ± 4
WISE 0359−5405	Y0	13.02	15	-0.177 ± 0.053	-0.930 ± 0.062	0.145 ± 0.039	3.7	$5.9^{+1.3}_{-0.8}$	
WISE 0410+1502	Y0	11.53	9	0.974 ± 0.079	-2.144 ± 0.072	0.233 ± 0.056	4.2	$4.2^{+1.2}_{-0.6}$	50 ± 10
WISE 0535−7500	$\geqslant$Y1	11.80	7	-0.310 ± 0.128	0.159 ± 0.092	0.250 ± 0.079	3.2	21^{+13}_{-11}	
WISE 1405+5534	Y0p?	9.16	9	-2.297 ± 0.096	0.212 ± 0.137	0.133 ± 0.081	1.6	>3.4	
WISE 1541−2250	Y0.5	15.21	9	-0.983 ± 0.111	-0.276 ± 0.116	-0.021 ± 0.094	<1	>6.0	
WISE 1738+2732	Y0	15.22	13	0.348 ± 0.071	-0.354 ± 0.055	0.066 ± 0.050	1.3	>6.0	
WISE 2056+1459	Y0	6.64	11	0.881 ± 0.057	0.544 ± 0.042	0.144 ± 0.044	3.3	$7.5^{+4.3}_{-1.8}$	
WISE 0254+0223	T8	5.67	11	2.578 ± 0.042	0.309 ± 0.050	0.185 ± 0.042	4.4	$4.9^{+1.0}_{-0.6}$	62 ± 10
WISE 1506+7027	T6	17.44	11	-1.241 ± 0.085	1.046 ± 0.064	0.310 ± 0.042	7.4	$3.4^{+0.7}_{-0.4}$	27 ± 4
WISE 1741+2553	T9	9.90	19	-0.495 ± 0.011	-1.472 ± 0.013	0.176 ± 0.026	6.8	$5.8^{+1.1}_{-0.6}$	45 ± 6

Notes. Columns represent the object name, spectral type, χ^2 of the parallax/proper motion fit to the estimated positions, number of degrees of freedom, proper motion in R.A. and decl., the maximum likelihood estimate of parallax and its statistical significance, most probable distance (corrected for Lutz–Kelker bias), and the tangential velocity. Distance lower limits are based on a 2σ criterion. Tangential velocities are quoted only for cases with parallax significance >4, otherwise the $V_{\rm tan}$ estimate becomes strongly biased toward the assumed a priori mean value of 30 km s^{-1}.

1971) using the positional uncertainties quoted in Table 3. The resulting estimates of proper motion and parallax and their associated uncertainties are given in Table 3, and the model fits with respect to the astrometry measurements are presented in Figures 1–3. The chi-squared values, χ^2, for the parameter fits in Table 3 are, for the most part, close to the number of degrees of freedom, $N_{\rm df}$, indicating reasonably good modeling of position uncertainties. Formally, the probability of exceeding χ^2 given $N_{\rm df}$ has a median value 0.29.

The parallaxes that we present are, strictly speaking, relative parallaxes since no correction has been made for the small parallaxes and proper motions of the reference stars, most of which are relatively nearby. However, the expected correction for such effects is only ∼2 mas (Dupuy & Liu 2012) which is at least an order of magnitude smaller than our typical astrometric uncertainties listed in Table 3, so in this error regime the distinction between relative and absolute parallaxes is unimportant.

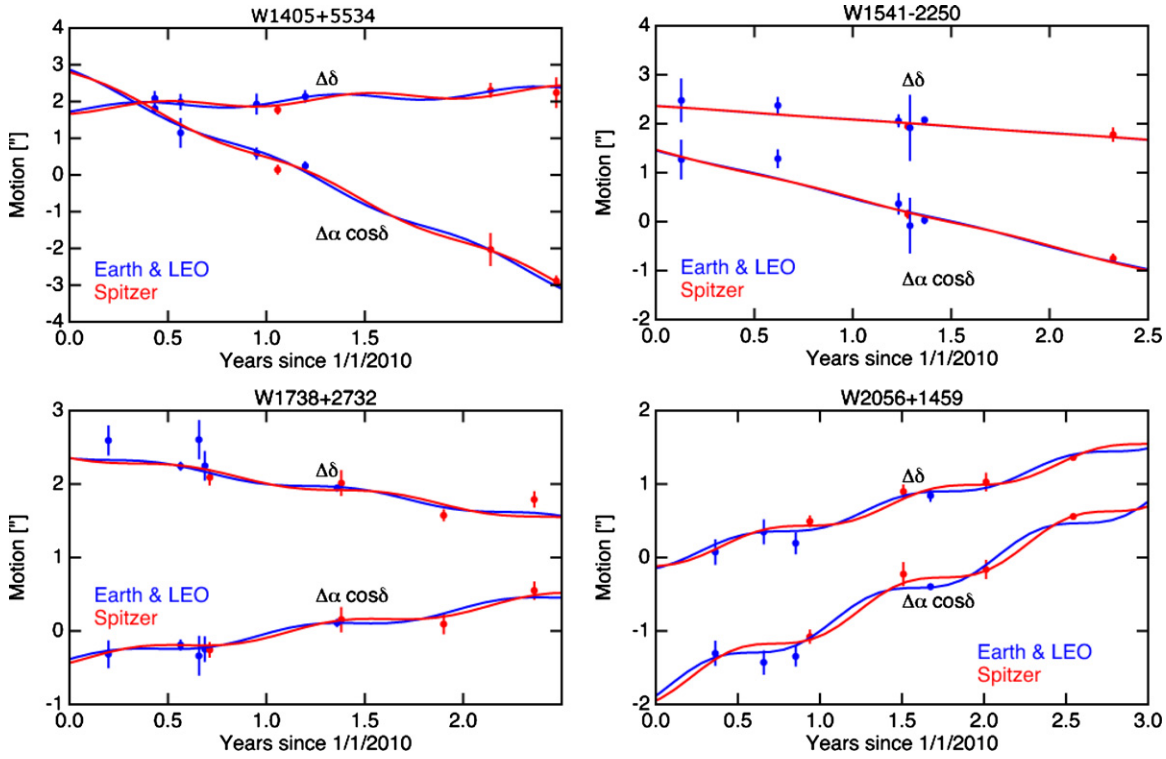

Figure 2. Proper motion and parallax fits to astrometry measurements of the remaining four Y dwarfs. Color convention is the same as for Figure 1.
(A color version of this figure is available in the online journal.)

In order to check to what extent our parallax and proper motion estimates may have been affected by systematic effects of focal-plane distortion not properly modeled by the statistical assumptions of the previous section, we have compared the rms residuals of the above fits (obtained using multiple reference stars) with those obtained using a single reference star for each brown dwarf, and found that there was no significant difference. This suggests that whatever residual focal-plane distortion errors exist, they are smaller than the random errors of source extraction.

We have converted our maximum likelihood estimates of parallax into most probable estimates of distance taking into account both the parallax measurements themselves and prior information. The latter includes an assumption that our objects are spatially distributed in a statistically uniform manner. Formally, that would imply that parallax values are distributed a priori as $P(\pi) \propto \pi^{-4}$; the singularity at zero would then lead to difficulties in estimating the a posteriori most probable π. Even though the zero parallax can be excluded on physical grounds, there is still a bias toward small values such that for S/N < 4, maximum likelihood parallax estimates become insignificant (Lutz & Kelker 1973). Fortunately there is additional prior information to alleviate this problem; small parallaxes (i.e., large distances) can be excluded if they are inconsistent with the observed proper motion based on an assumed velocity dispersion of the objects being studied (Thorstensen 2003).

With these considerations in mind, our estimates of distance, d, are based on the following assumptions:

1. Our maximum likelihood parallax values, $\pi_{\rm ML}$, are distributed as Gaussians with standard deviation σ_π.
2. Our objects are distributed spatially in a statistically uniform way, so that the a priori probability density distribution of d is proportional to d^2.
3. The distribution of tangential velocities of Y dwarfs in the solar neighborhood can be described by a Gaussian random process with mean and standard deviation $\bar{V}$ and σ_V, respectively; we assume the values $\bar{V} = 30$ km s^{-1} and $\sigma_V = 20$ km s^{-1} respectively, representative of previous observations of T dwarfs (Faherty et al. 2009).

We then obtain the most probable distance, $\hat{d}$, by maximizing the conditional probability density $P(d|\pi_{\rm ML}, \mu_{\rm ML})$, which from Bayes' rule can be expressed by

$$P(d|\pi_{\rm ML}, \mu_{\rm ML}) \propto d^2 \exp\left(-(\mu_{\rm ML} d - \bar{V})^2/(2\sigma_V^2)\right) \times \exp\left(-(\pi_{\rm ML} - 1/d)^2/(2\sigma_\pi^2)\right), \quad (9)$$

where $\mu_{\rm ML}$ represents the magnitude of our maximum likelihood estimate of proper motion. Our distance estimates are presented in Column 9 of Table 3. The error bars correspond to the 0.159 and 0.841 points of the cumulative distribution with respect to $P(d|\pi_{\rm ML}, \mu_{\rm ML})$.

5. DISCUSSION

As is evident from Table 1, our observations represent a mixed bag in terms of telescopes (and hence spatial resolution) and time sampling since they were not specifically designed for astrometry, but rather for follow-up photometry of brown dwarfs detected by *WISE*. The quality of the observations was quite varied, and not always with sufficient pixel subsampling for the estimation of the high-quality PSFs necessary for astrometry. In the case of *Spitzer*, for example, each observation consisted of a set of only five dithered images.

In addition, the time sampling of the parallactic cadence is of key importance in the estimation of parallax. The ideal sampling involves observations at solar elongation angles of $\pm 90^\circ$,

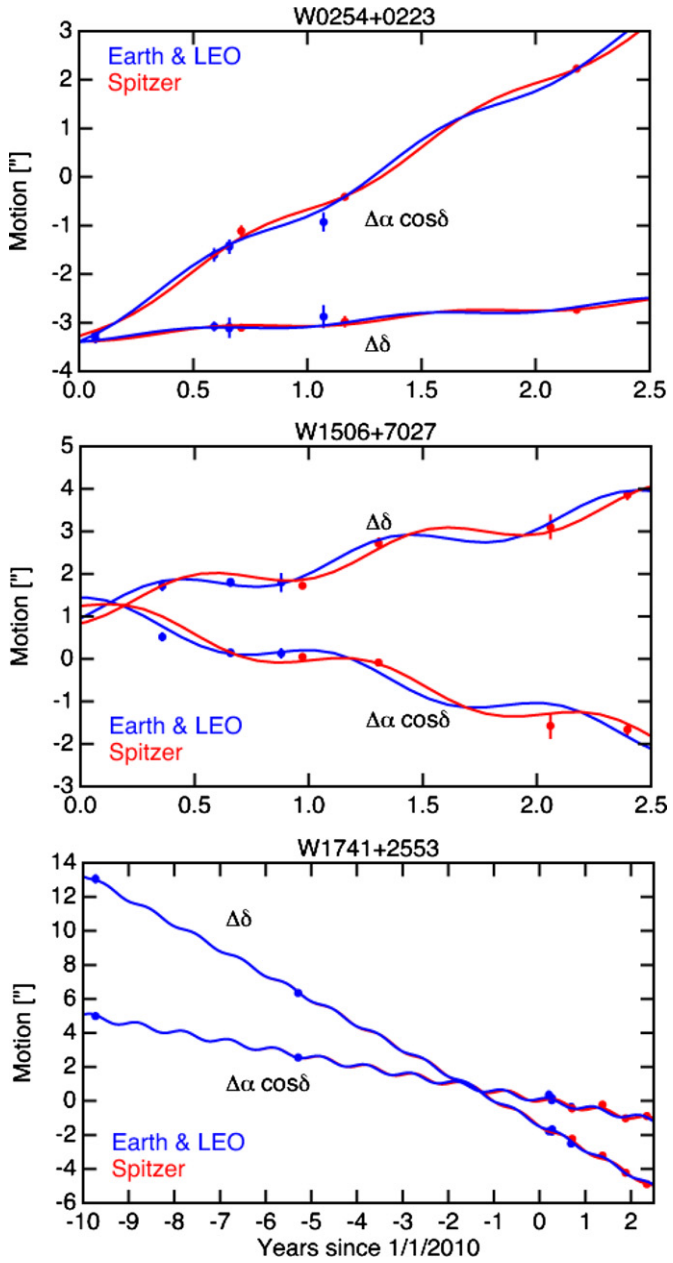

Figure 3. Proper motion and parallax fits to astrometry measurements of the three T dwarfs. Color convention is the same as for Figure 1.

(A color version of this figure is available in the online journal.)

and this is achieved by *WISE*, albeit with large position errors (typically ∼0.″1–0.″3). These elongation angles are critical for an object on the ecliptic and less important at high ecliptic latitudes. For the parallax measurements described here, the worst example of poor sampling was WISE 1541−2250 for which all of the non-*WISE* observations were in one quadrant of solar elongation angle (see Column 8 of Table 1), so it is not surprising that the observations did not yield a significant parallax measurement. The previous measurement, corresponding to an estimated distance range of 2.2–4.1 pc (Kirkpatrick et al. 2011), was based on even fewer observations and furthermore used position estimates for which the PSF errors were somewhat underestimated. Our present result of >6 pc therefore supercedes that estimate, but this object should clearly be revisited once a more optimal sampling of the parallactic ellipse has been obtained. By and large, however, there is a good correlation between the sampling cadence and the quality of the parallax estimate; future observations will be optimized both for image quality and cadence.

Nevertheless, significant parallaxes (S/N > 3) have been obtained for five of the eight Y dwarfs and all three of the T dwarfs, thus providing distance estimates. Also, we have combined the latter with our proper motion estimates to yield tangential velocities, $V_{\rm tan}$. Of course, our estimated values, $\hat{d}$ and $\hat{V}_{\rm tan}$, are somewhat dependent on the assumed prior distribution of $V_{\rm tan}$ in Equation (9), and the assumed similarity to the T dwarf distribution may not be valid if the Y dwarfs represent a significantly older population. In order to assess the sensitivity to this assumption, the distance estimates were repeated using a σ_V of 100 km s^{-1}. It was found that for a parallax significance S/N > 4, the increase in σ_V led to no more than a 20% change (always in the positive direction) in $\hat{d}$ and hence $\hat{V}_{\rm tan}$. For lower values of S/N, $\hat{V}_{\rm tan}$ becomes biased toward the a priori value, $\bar{V}$, in Equation (9). Thus in Table 3 we quote $\hat{V}_{\rm tan}$ values only for S/N > 4. Similarly, for S/N < 4 the reliability of our distance estimates is dependent on the validity of the assumptions regarding the a priori distribution of $V_{\rm tan}$.

On this basis we obtained significant values of $V_{\rm tan}$ for two of our Y dwarfs; both are <100 km s^{-1}, suggesting membership in the thin disk population (Dupuy & Liu 2012). Similar analysis techniques, both in terms of the source extraction and parallax estimation, were used by Wright et al. (2012) to estimate the distance to the T8.5 object WISE 1118+3125, inferred (with the aid of its observed common proper motion) to be a member of the ξ UMa system, with excellent agreement with the known distance of that system.

The distance estimates for the present sample, all of which are $\gtrsim$3 pc, have enabled the estimation of absolute magnitudes. These indicate that luminosities plummet at the T/Y boundary (Kirkpatrick et al. 2012) as illustrated by Figures 4 and 5, which represent updated versions of the absolute magnitude versus spectral-type plots from the latter work. The steep decrease may at least partially account for the apparent scatter in absolute magnitudes of objects of the same spectral type, since in the Y0 regime an error of half a spectral type apparently corresponds to more than a magnitude difference in luminosity. More data will be required to make a definitive statement, however.

The absolute magnitudes also provide valuable guidance for models in the ultra-cool regime. To this end we have compared our observational results with model-based and empirical predictions using plots of absolute magnitude as a function of color, as shown in Figure 6. The M_J versus $J-H$ plot in the upper panel shows that the Y dwarfs continue the trend set by the L and T dwarfs based on the parallax observations of Dupuy & Liu (2012). A key feature is the turnover in the blueward progression of the color at $M_J \sim 16$, at considerably redder $J-H$ than predicted by cloud-free models (Saumon & Marley 2008) as illustrated by the solid curve. Such behavior is also apparent in the color–magnitude diagrams for cloud-free models presented by Leggett et al. (2010). The dotted/dashed curves in Figure 6 represent models incorporating the effect of clouds containing various amounts of Cr, MnS, Na_2S, ZnS, and KCl condensates (Morley et al. 2012), as indicated by the sedimentation efficiency parameter, $f_{\rm sed}$; lower values correspond to optically thicker clouds. It is apparent that these models can account at least partly for the relative redness of some of the $J-H$ colors, but they predict a blueward hook for temperatures below

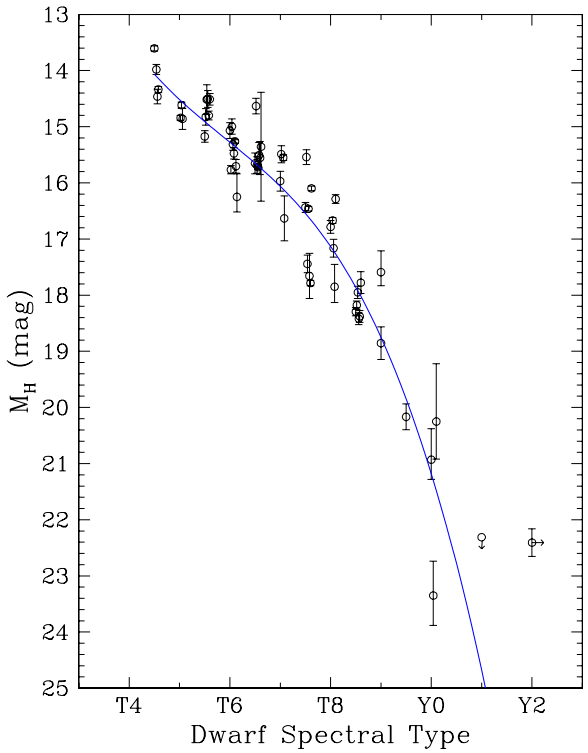

Figure 4. Absolute H magnitude as a function of spectral type. This is a revised version of the corresponding figure in Kirkpatrick et al. (2012) and includes the objects from the present paper and the new parallax estimate for WISE 1828+2650 (Beichman et al. 2012). The blue curve represents the relation used by Kirkpatrick et al. (2012), which appears still to be an accurate representation of the absolute magnitude vs. spectral type trend despite the fact that our results have been revised since the Kirkpatrick et al. paper was published.

(A color version of this figure is available in the online journal.)

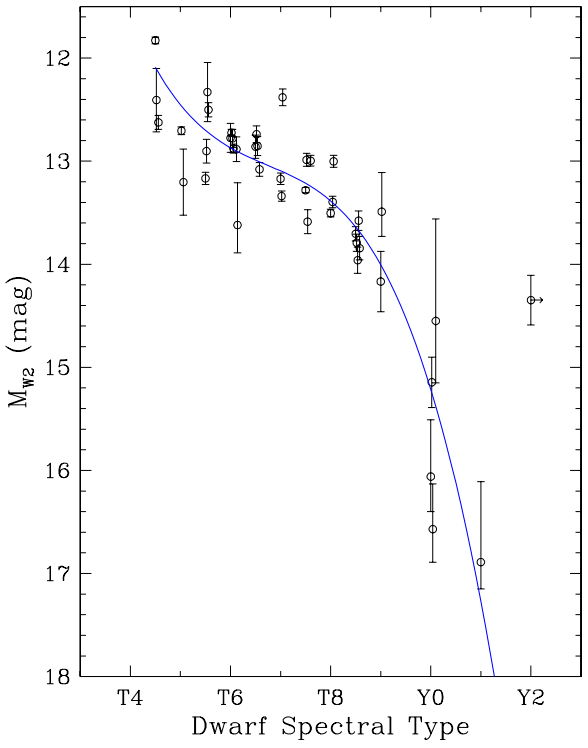

Figure 5. Absolute $W2$ magnitude as a function of spectral type. As with Figure 4 it is taken from Kirkpatrick et al. (2012) except for the inclusion of the objects from the present paper. It also includes WISE 1639−6847 (Tinney et al. 2012).

(A color version of this figure is available in the online journal.)

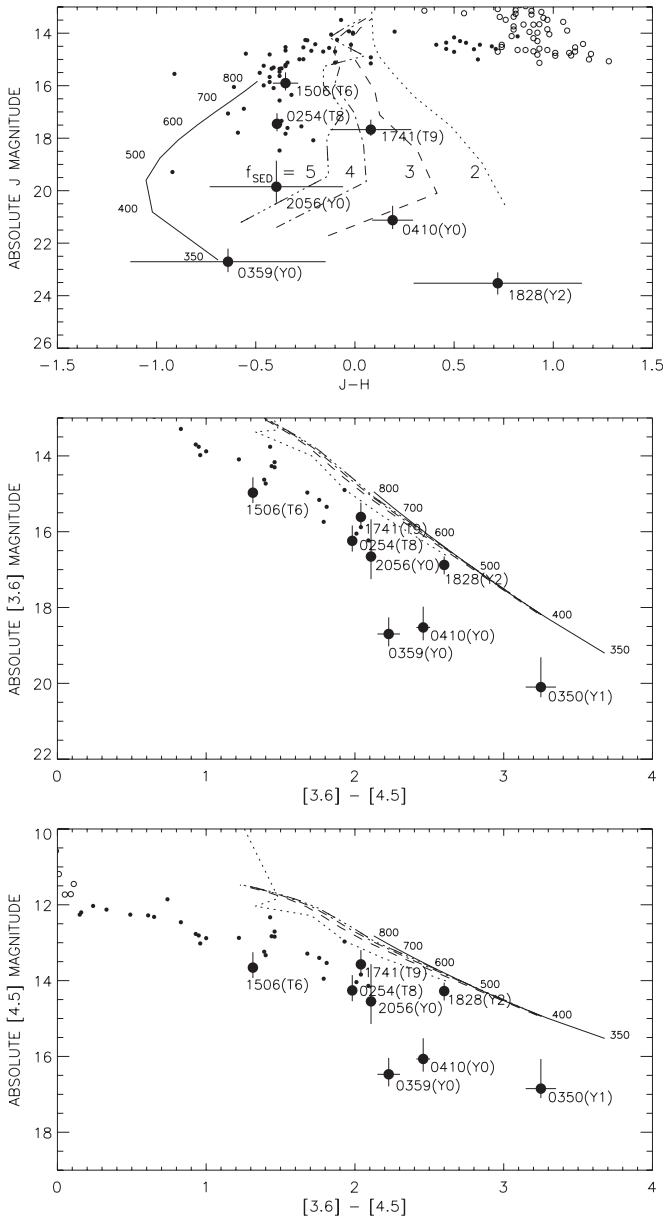

Figure 6. Absolute magnitude as a function of color. Large filled circles with error bars represent the objects from this paper, plus WISE 1828+2650 (Beichman et al. 2012). Also included are the L and T dwarfs from Dupuy & Liu (2012), represented by open circles and small filled circles, respectively. For comparison, model curves are overplotted. The solid curve represents a cloud-free model from Saumon & Marley (2008), assuming $g = 1000$ m s^{-2}, $K_{zz} = 0$. The numbers along this line represent the assumed values of effective temperature [K]. Also plotted (dashed/dotted lines) are four cloudy models from Morley et al. (2012) with the same assumed g and K_{zz}, and with various values of the sedimentation efficiency parameter, $f_{\rm sed}$, as indicated.

400 K, which does not appear to be matched by the observations. Perhaps some of the scatter in $J - H$ colors in Figure 6 might be explained in terms of a patchy cloud model; it is also possible that the inclusion of water clouds might improve consistency with the observations.

Figure 6 does show reasonable consistency between observations and models based on IRAC colors, i.e., $M_{[3.6]}$ and $M_{[4.5]}$ as a function of the [3.6]–[4.5] color. The only major discrepancy is that WISE 1828+2650, whose effective temperature is believed to be ∼300 K, falls at a location more indicative of 500 K on these plots.

We thank C. Morley for providing the results of model calculations and also the referee for very helpful comments. This publication makes use of data products from the *Wide-field Infrared Survey Explorer*, which is a joint project of the University of California, Los Angeles, and the Jet Propulsion Laboratory/California Institute of Technology, funded by the National Aeronautics and Space Administration. This work is based in part on observations made with the Spitzer Space Telescope, which is operated by the Jet Propulsion Laboratory, California Institute of Technology, under a contract with NASA. Support for this work was provided by NASA through an award issued to programs 70062 and 80109 by JPL/Caltech. This work is also based in part on observations made with the NASA/ESA *Hubble Space Telescope*, obtained at the Space Telescope Science Institute, which is operated by the Association of Universities for Research in Astronomy, Inc., under NASA contract NAS 5-26555. These observations are associated with program 12330, support for which was provided by NASA through a grant from the Space Telescope Science Institute. This paper also includes data gathered with the 6.5 meter Magellan Telescopes located at Las Campanas Observatory, Chile. This research has made use of the NASA/IPAC Infrared Science Archive (IRSA), which is operated by the Jet Propulsion Laboratory, California Institute of Technology, under contract with the National Aeronautics and Space Administration, and also the SIMBAD database, operated at CDS, Strasbourg, France.

REFERENCES

Beichman, C., et al. 2012, ApJ, submitted
Bloom, J. S., et al. 2006, in ASP Conf. Ser. 351, Astronomical Data Analysis Software and Systems XV, ed. C. Gabriel, C. Arviset, D. Ponz, & E. Solano (San Francisco, CA: ASP), 751
Burgasser, A. J., Marley, M. S., Ackerman, A. S., et al. 2002, ApJL, 571, 151
Cushing, M. C., Kirkpatrick, J. D., Gelino, C. R., et al. 2011, ApJ, 743, 50
Cutri, R. M., et al. 2003, 2MASS All Sky Catalog of Point Sources (http://irsa.ipac.caltech.edu/applications/Gator/)
Dahn, C. C., Harris, H. C., Vrba, F. J., et al. 2002, AJ, 124, 1170
Dupuy, T. J., & Liu, M. C. 2012, ApJS, 201, 19
Epchtein, E. N., de Batz, B., Capoani, L., et al. 1997, Msngr, 87, 27
Faherty, J. K., Burgasser, A. J., Cruz, K. L., et al. 2009, AJ, 137, 1
Faherty, J. K., Burgasser, A. J., Walter, F. M., et al. 2012, ApJ, 752, 56
Fazio, G. G., Hora, J. L., Allen, L. E., et al. 2004, ApJS, 154, 10
Kanneganti, S., Park, C., Skrutskie, M. F., et al. 2009, PASP, 121, 885
Kirkpatrick, J. D., Cushing, M. C., Gelino, C. R., et al. 2011, ApJS, 197, 19
Kirkpatrick, J. D., Gelino, C. R., Cushing, M. C., et al. 2012, ApJ, 753, 156
Leggett, S. K., Burningham, B., Saumon, D., et al. 2010, ApJ, 710, 1627
Looper, D. L., Gelino, C. R., Burgasser, A. J., & Kirkpatrick, J. D. 2008, ApJL, 685, 1183
Lutz, T. E., & Kelker, D. H. 1973, PASP, 85, 573
Marley, M. S., Saumon, D., & Goldblatt, C. 2010, ApJ, 723, 117
Marocco, F., Smart, R. L., Jones, H. R. A., et al. 2010, A&A, 524, 38
Martini, P., Persson, S. E., Murphy, D. C., et al. 2004, Proc. SPIE, 5492, 1653
McLeod, B. A., Fabricant, D., Geary, J., et al. 2004, Proc. SPIE, 5492, 1306
Morley, C. V., Fortney, J. J., Marley, M. S., et al. 2012, ApJ, 756, 172
Saumon, D., & Marley, M. S. 2008, ApJ, 689, 1327
Simcoe, R. A., Burgasser, A. J., Bernstein, R. A., et al. 2008, Proc. SPIE, 7014, 70140U
Simcoe, R. A., Burgasser, A. J., Bochanski, J. J., et al. 2010, Proc. SPIE, 7735, 773514
Skrutskie, M. F., Cutri, R. M., Stiening, R., et al. 2006, AJ, 131, 1163
Straughn, A. N., Kuntschner, H., Kümmel, M., et al. 2011, AJ, 141, 14
Swaters, R. A., Valdes, F., & Dickinson, M. E. 2009, in ASP Conf. Ser. 411, Astronomical Data Analysis Software and Systtems XVIII, ed. D. A. Bohlender, D. Durand, & P. Dowler (San Francisco, CA: ASP), 506
Thorstensen, J. R. 2003, AJ, 126, 3017
Tinney, C. G., Burgasser, A. J., & Kirkpatrick, J. D. 2003, AJ, 126, 975
Tinney, C. G., Faherty, J. K., Kirkpatrick, J. D., et al. 2012, ApJ, 759, 60
Vrba, F. J., Henden, A. A., Luginbuhl, C. B., et al. 2004, AJ, 127, 2948
Werner, M. W., Roellig, T. L., Low, F. J., et al. 2004, ApJS, 154, 1
Whalen, A. D. 1971, Detection of Signals in Noise (New York: Academic)
Wilson, J. C., Eikenberry, S. S., Henderson, C. P., et al. 2003, Proc. SPIE, 4841, 451
Wright, E. L., Eisenhardt, P. R. M., Mainzer, A. K., et al. 2010, AJ, 140, 1868
Wright, E. L., et al. 2012, AJ, submitted (arXiv:1203.5764)
York, D. G., Adelman, J., Anderson, J. E., Jr., et al. 2000, AJ, 120, 1579